Examination of nuclear chirality with a magnetic moment measurement of the $I = 9$ isomeric state in ^{128}Cs

E. Grodner,[1,*] M. Kowalczyk,[2] M. Kisieliński,[2] J. Srebrny,[2] L. Próchniak,[2] Ch. Droste,[3] S. G. Rohoziński,[3,†] Q. B. Chen,[4] M. Ionescu-Bujor,[5] C. A. Ur,[6] F. Recchia,[6] J. Meng,[7,8,9] S. Q. Zhang,[7] P. W. Zhao,[7] G. Georgiev,[10] R. Lozeva,[10] E. Fiori,[10] S. Aydin,[11] and A. Nałęcz-Jawecki[1]

[1]*National Centre for Nuclear Research, 05-540 Świerk, Poland*
[2]*Heavy Ion Laboratory, University of Warsaw, 02-093 Warsaw, Poland*
[3]*Faculty of Physics, University of Warsaw, 02-093 Warsaw, Poland*
[4]*Department of Physics, East China Normal University, Shanghai 200241, China*
[5]*Horia Hulubei National Institute for Physics and Nuclear Engineering, 077125 Bucharest, Romania*
[6]*Instituto Nationale di Fisica Nucleare, I-35131 Padova, Italy*
[7]*State Key Laboratory of Nuclear Physics and Technology, School of Physics, Peking University, Beijing 100871, China*
[8]*School of Physics, Beihang University, Beijing 102206, China*
[9]*Yukawa Institute for Theoretical Physics, Kyoto University, Kyoto 606-8502, Japan*
[10]*IJCLab, CNRS/IN2P3, Université Paris-Saclay, 91405 Orsay, France*
[11]*Department of Natural and Mathematical Sciences, Faculty of Engineering, Tarsus University, 33480 Mersin, Turkey*

(Received 23 December 2021; accepted 27 May 2022; published 28 July 2022)

The g factor of the isomeric $I = 9^+$ bandhead of the yrast states in ^{128}Cs is obtained from the time differential perturbed angular distribution measurement performed with the electromagnet at IPN Orsay. An external magnetic field of 2.146 T at the target position was attained with GAMIPE reaction chamber surrounded by four high-purity germanium detectors, of which two were low-energy photon spectrometer type. The results are in accordance with $\pi h_{11/2} \otimes \nu h_{11/2}^{-1}$ $I = 9^+$ bandhead assignment and are discussed in the context of chiral interpretation of the ^{128}Cs nucleus as a composition of the odd proton, odd neutron, and even-even core with their angular momentum vectors. The obtained g-factor value was compared with predictions of the particle-rotor model. The experimental g factor corresponds to the nonchiral geometry of the isomeric bandhead. This observation indicates the existence of the chiral critical frequency in ^{128}Cs and may explain the absence of the chiral doublet members for $I < 13\hbar$.

DOI: 10.1103/PhysRevC.106.014318

I. INTRODUCTION

The ^{128}Cs nucleus studied in this paper belongs to a group of nuclei around $A \approx 130$ in which the phenomenon of nuclear chirality [1] has been reported through the observation of chiral doublet states [2] and specific selection rules for the gamma transitions between these states [3–6].

The chiral partner bands in the ^{128}Cs nucleus are described as the coupling of three components: an even-even core with angular momentum j_R and two odd nucleons in $\pi h_{11/2} \otimes \nu h_{11/2}^{-1}$ configuration with angular momenta j_p and j_n, respectively. The reported observables serve as an indirect sign of the chiral geometry formed in the ^{128}Cs nucleus, where the three angular momentum vectors span the three-dimensional space.

In the ideal geometry the j_R, j_p, and j_n vectors are mutually perpendicular and build either a right- or left-handed reference frame corresponding to left-handed $|L\rangle$ or right-handed $|R\rangle$ intrinsic nuclear states. The mechanism of the spontaneous chiral symmetry breaking in a nuclear system occurs when an excited nucleus cools down and at some point chooses spontaneously one of the two intrinsic states. The nucleus does not stay in the chosen intrinsic configuration since it is not its eigenstate. Tunneling between $|L\rangle$ and $|R\rangle$ configurations takes place with a period much shorter than the time required for the gamma quantum emission to occur from the excited states of the nucleus. This is why the intrinsic states with specified handedness cannot directly be observed in gamma spectroscopy experiments. Instead of the $|L\rangle$ and $|R\rangle$ intrinsic configurations their projections onto the eigenstates of the nucleus, i.e., chiral doublets, are seen through observation of the emitted gamma rays. Therefore, the handedness of the three angular momentum vectors is fundamentally hidden for nuclear spectroscopy investigations where chiral doublets and other associated observables indicate the existence of spontaneous chiral symmetry breaking.

Even though the handedness cannot be observed directly, the magnetic dipole moment allows one to study the nuclear chirality regardless of the handedness of the nucleus. It turns out that the value of the magnetic dipole moment and the

*Corresponding author: grodner.ernest@gmail.com
†Deceased.

 ©2022 American Physical Society

corresponding value of the g factor are functions of the geometry formed by the three angular momentum vectors through their scalar products. These products are symmetric with respect to handedness, giving nonzero values in the symmetric eigenstates with mixed handedness. Therefore, the value of the g factor may give information on whether the three angular momentum vectors span a three-dimensional space (chiral configuration) or lie in one plane (planar or nonchiral configuration) regardless of the handedness of the intrinsic dynamical state.

In this paper, the g-factor value of the isomeric $I = 9^+$ bandhead of the yrast states in ^{128}Cs was measured with the classical time dependent perturbed angular distribution (TDPAD) method. It is the lowest lying state in the rotational yrast band, being one of the chiral partners built on the $\pi h_{11/2} \otimes \nu h^{-1}_{11/2}$ configuration. The chiral character of the partner bands in ^{128}Cs has been observed in states with significant nuclear rotation corresponding to spins higher than $13\hbar$ [3]. With decreasing nuclear rotation the yrare band is not observed, leaving room for two hypotheses, one of which assumes that the nuclear chirality persists at low rotational frequency although low spins of the yrare band are not fed by fusion reaction mechanism. In such a case the g-factor value of the bandhead should correspond to a chiral geometry of the three-component system. The other hypothesis states that there is a phase transition suppressing the chiral geometry at low rotational frequency. This may happen below the chiral critical frequency [7] predicted by the tilted axis cranking model. Existence of this critical frequency may prevent the chiral geometry from developing in energy favored nuclear states. Thus a nonchiral or planar character of the bandhead is expected. This article details the experimental as well as the theoretical methods for the magnetic moment measurement and its interpretation, the brief results of which were published in [8]. The principle of the measurement and methods of the data analysis are described in Secs. II and III. Sections IV and V contain analytical considerations of the magnetic moment as formed by single coupling schemes of two or three angular momentum vectors, while Secs. VI and VII present detailed calculation and interpretation in the frame of the many-particle–many-hole particle rotor model.

II. EXPERIMENTAL SETUP

The ^{128}Cs nucleus was produced in the ^{122}Sn(^{10}B, $4n$) ^{128}Cs fusion-evaporation reaction at 55 MeV beam energy. A pulsed ^{10}B beam with 1 ns bursts and 400 ns repetition period was developed by the Tandem accelerator at IPN Orsay. Single gamma quanta were registered by two low-energy photon spectrometer (LEPS) detectors placed at $\pm 45^\circ$ with respect to the beam axis. The decay of the $I = 9^+$ isomeric state was studied using off-beam sorted coincidences of gamma quanta registered between beam pulses [9]. The relevant part of the level scheme is shown in Fig. 1, where 14 prompt gamma transitions follow the $I = 9^+$ isomeric state decay.

These transitions were subject of the TDPAD measurement with an external magnetic field produced by an electromagnet at IPN Orsay. Interaction of the external magnetic field and the magnetic moment associated with a nuclear state leads to

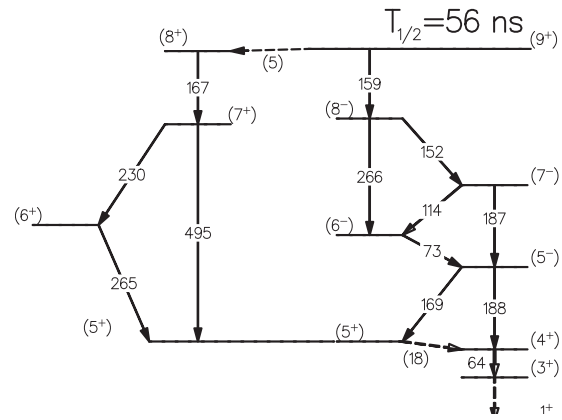

FIG. 1. Relevant part of the level scheme of ^{128}Cs obtained in Ref. [9]. The decay of the isomeric state is reconstructed from coincidences collected between beam pulses and from prompt-delayed gamma coincidences. The two transitions represented by dashed lines, 18 and 5 keV, are below the sensitivity threshold of the experiment due to high electron-conversion decay mode.

precession of the nuclear angular momentum vector. To get the g-factor value with high precession at least half circumvolution of the nuclear spin should occur in the period of the isomeric level lifetime. The Larmor frequency of precession $\boldsymbol{\omega}_L = -g\mathbf{B}\mu_N/\hbar$ is proportional to the nuclear g factor and the external magnetic field. The half-life of the isomeric state $T_{1/2} = 56$ ns [9] together with theoretical estimates of its g factor $g \approx 0.5$ [10] gave the required magnetic field $B \approx 2$ T for a half circumvolution within a 50 ns period. The magnetic field of around 0.7 T attainable at the electromagnet was magnified with the help of the GAMIPE reaction chamber of NIPNE (National Institute for Physics and Nuclear Engineering, Romania); see Fig. 2.

The GAMIPE chamber equipped with cone-shaped iron poles allowed us to focus the magnetic field, that reached 2.146 T in the target position. In Fig. 2 the uniformity of the magnetic field is presented as a plot of the B field vs

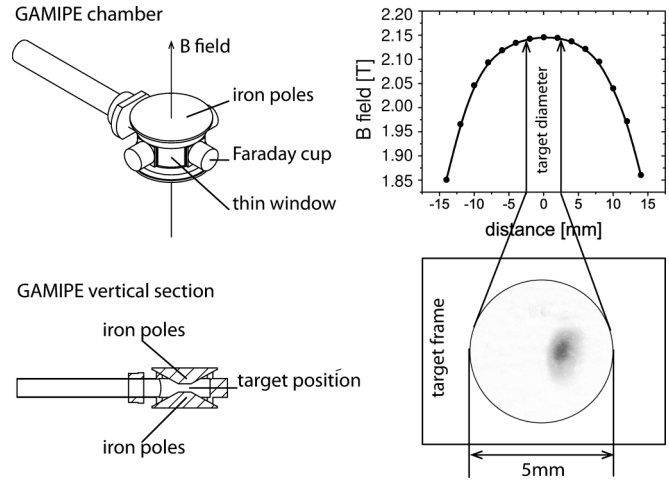

FIG. 2. GAMIPE reaction chamber, the B field uniformity, and the beam spot.

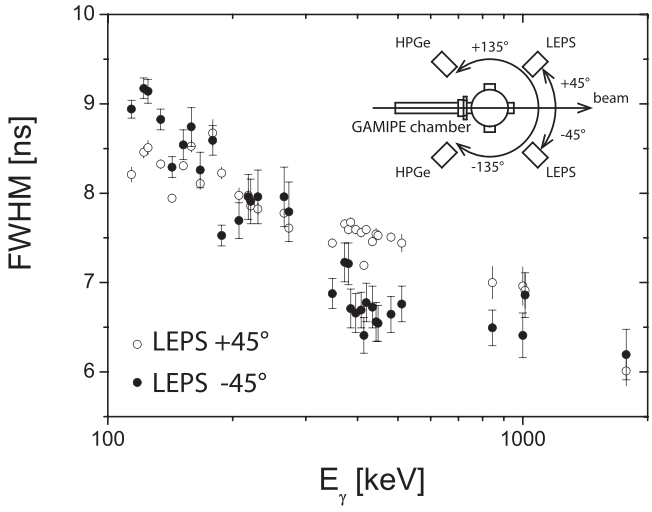

FIG. 3. Experimental geometry and timing resolution.

horizontal distance from the center of the chamber. One can see that the magnetic field changes about 1.2% within the ±5 mm distance that is the target diameter. This change had to be taken into account since the projectiles were deflected from the center point of the target by the applied magnetic field. The final position of the 1 mm^2 beam spot in the target plane was determined by burning a beam fleck in a paper layer placed instead of the target foil (cf. Fig. 2). This allows precise measurement of the magnetic field $B = 2.146$ T at the beam spot before and after the experiment. Figure 3 shows the geometry of the experimental setup.

The ^{122}Sn(^{10}B, $4n$)^{128}Cs reaction populated the aligned states of ^{128}Cs recoils that stopped in the Sn target of 22 mg/cm^2 thickness. Small initial velocity $v \approx 0.01c$ [3] as well as short stopping time $t_{\text{stop}} \approx 1$ ps of recoils ensures that the decay of the isomeric state happens mostly from ^{128}Cs nuclei at rest. Therefore, both the spin alignment and the distribution of the gamma radiation had a mirror symmetry with respect to the plane perpendicular to the beam direction, which is shown schematically in Fig. 4. Precession of the angular distribution

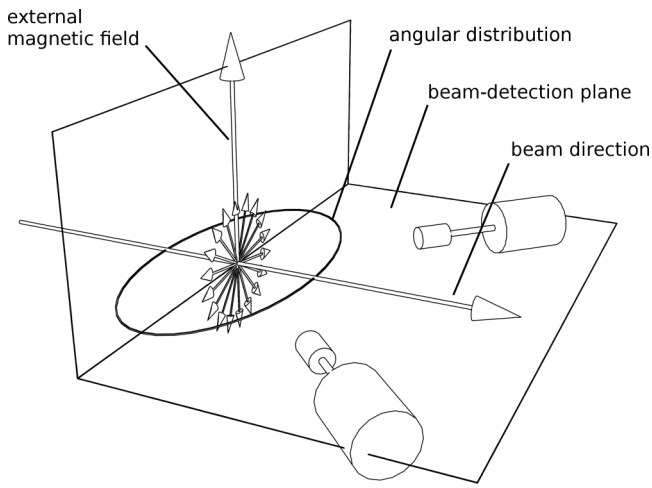

FIG. 4. Experimental setup arrangement.

with a frequency ω_L was observed by an intensity modulation, whose frequency was twice higher as a result of the mirror symmetry. The modulation period of around 50 ns was registered by two low-energy photon spectrometers (LEPS) of Laboratori Nazionali di Legnaro. As shown in Fig. 4, the two LEPS detectors were placed at angles ±45° with respect to the beam axis, forming a beam-detection plane with the magnetic field perpendicular to it.

The excellent time resolution of LEPS detectors vs γ-quanta energy, shown in Fig. 3, is gained at the expense of detection efficiency of high-energy electromagnetic radiation. Therefore two other Ge-spectrometers—standard HPGe (high purity Ge) detectors with beryllium window and 35% relative efficiency—were placed at angles ±135° with respect to the beam axis in order to increase the detection efficiency for high-energy gammas. Neither of the four Ge detectors was equipped with ACS (anti-Compton shielding). Figure 3 shows that the time resolution of LEPS detectors in the present experiment is around 8 ns for $E_\gamma \approx 120$ keV and drops to around 6 ns for $E_\gamma \approx 1700$ keV. Signal-processing electronics, i.e., spectroscopic amplifiers, TAC (time-to-amplitude converter), CFD (constant fraction discriminator), TFA (timing filter amplifier), and two HPGe detectors with 35% efficiency were delivered by the Heavy Ion Laboratory of the University of Warsaw while event signals readout in a single gamma mode was done using the Orsay data acquisition system.

For a single gamma quantum, information on its energy (taken from the spectroscopic amplifiers) and registration time with respect to beam pulse (taken from TAC) were collected. For an individual Ge detector the associated CFD logic output signal was used as the TAC start input while the logic signal from the unit forming the pulsed beam structure of the TANDEM accelerator was used as the TAC stop input.

Single gamma quanta were collected during 5 days the beam time. The energy gated time spectra for the g-factor evaluation were then constructed in off-beam mode using HIL (Heavy Ion Laboratory) sorting software.

III. DATA ANALYSIS AND RESULTS

The $I = 9^+$ isomeric state decays via 167 and 159 keV transitions which are followed by emission of another 12 gamma quanta [9]. Modulated intensity was observed for all transitions below the isomer except 18 and 5 keV lines which are below the sensitivity threshold of the experiment due to high electron-conversion decay mode. The intensity modulation of the Compton background can mimic the modulation effect for the given transition. Therefore, background subtracted time spectra were produced where a time spectrum gated on the background was subtracted from the time spectrum gated on a gamma-ray peak.

Figure 5 illustrates the time spectrum gated on the $E =$ 152 keV peak with and without background subtraction together with the time spectrum of the Compton background. The modulated intensity follows a straight line on a logarithmic scale, indicating proper background subtraction. Background subtracted oscillation spectra were found for 11 gamma lines associated with the isomeric state decay.

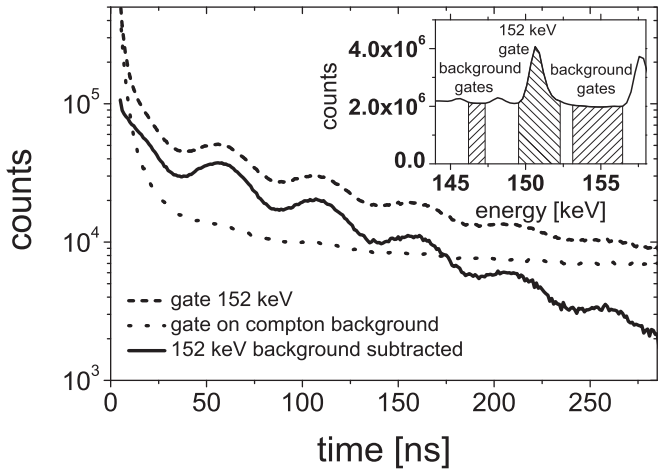

FIG. 5. Background subtraction from the time spectrum of 152 keV peak.

A rotating angular distribution inherits the symmetry of the rotating spin alignment, giving intensity modulations of opposite phase observed by the LEPS detectors placed at a right angle in the beam-detection plane. All oscillation spectra observed in the present experiment are shown in Fig. 6, where the spectra were normalized by multiplying the -45° LEPS spectra by a factor of 2.4.

One can see that oscillation of the 114 keV transition in the first 70 ns after the beam pulse is disturbed by an overlapping unidentified 115 keV peak. The 115 keV line is observed in coincidence with a 122 keV gamma which presents much shorter half-life than the 56 ns half-life of the $I = 9^+$ isomeric state. Therefore, the analysis of the 114 keV oscillations was performed for gammas registered after the 70 ns decay of the overlapping transition. Rotation of the angular distribution leads to the modulation of the gamma intensity observed by a detector in the beam detection plane according to the formula

$$I(\theta, t) = I_0 e^{-t/\tau}\{1 + \alpha_2(t)Q_2A_2P_2[\cos(\theta - \omega_L t)] + \alpha_4(t)Q_4A_4P_4[\cos(\theta - \omega_L t)]\}, \quad (1)$$

where A_2, A_4 are the gamma angular distribution coefficients, Q and $\alpha(t)$ the attenuation factors due to the finite detector size and time dependent spin alignment, τ the $I = 9^+$ isomeric state lifetime, and ω_L the Larmor frequency of precession. Only even Legendre polynomials P_2 and P_4 are present in the formula (1) as a result of the mirror symmetry of the initial gamma angular distribution. With an assumption of identical detector properties one gets the same Q attenuation factors for both detectors. This allows one to get a precise value of the Larmor frequency by constructing a modulation ratio spectra. A modulation ratio of the detectors placed at a right angle is defined as

$$R(t) = \frac{I(-45^\circ, t) - I(+45^\circ, t)}{I(-45^\circ, t) + I(+45^\circ, t)}, \quad (2)$$

where the numerator becomes

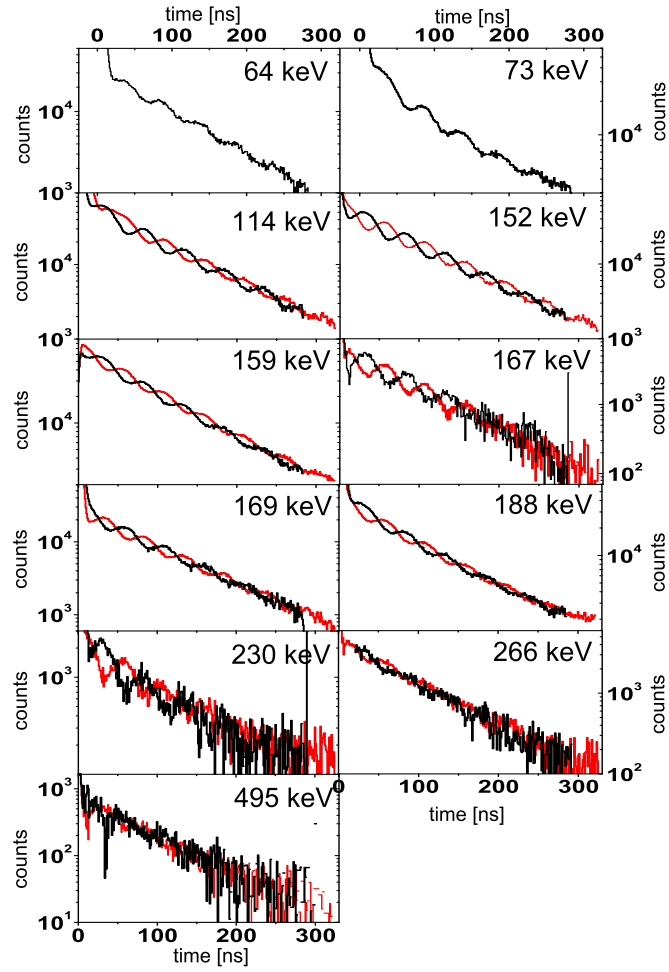

FIG. 6. Intensity oscillation spectra registered by LEPS detectors. Black lines shows the intensity registered at $+45^\circ$ with respect to beam axis while red lines show the intensity seen at -45°. The intensity curves were normalized by multiplying the -45° spectrum by factor of 2.4.

$$I(-45^\circ, t) - I(+45^\circ, t) = I_0 e^{-t/\tau}\left[\frac{3}{2}\alpha_2(t)Q_2A_2 + \frac{10}{16}\alpha_4(t)Q_4A_4\right]\cos[2(-45^\circ - \omega_L t)] \quad (3)$$

while the denominator simplifies to

$$I(-45^\circ, t) + I(+45^\circ, t) = I_0 e^{-t/\tau}\left[2 + \frac{1}{2}\alpha_2(t)Q_2A_2 + \frac{1}{16}\alpha_4(t)Q_4A_4\{35\cos^2[2(-45^\circ - \omega_L t)] - 13\}\right]. \quad (4)$$

For the assumption of identical detectors and small A_4 coefficients, one gets an approximate modulation ratio of the form

$$R(t) \approx \frac{-3\alpha_2(t)Q_2A_2\sin(2\omega_L t - \phi)}{4 + \alpha_2(t)Q_2A_2}, \quad (5)$$

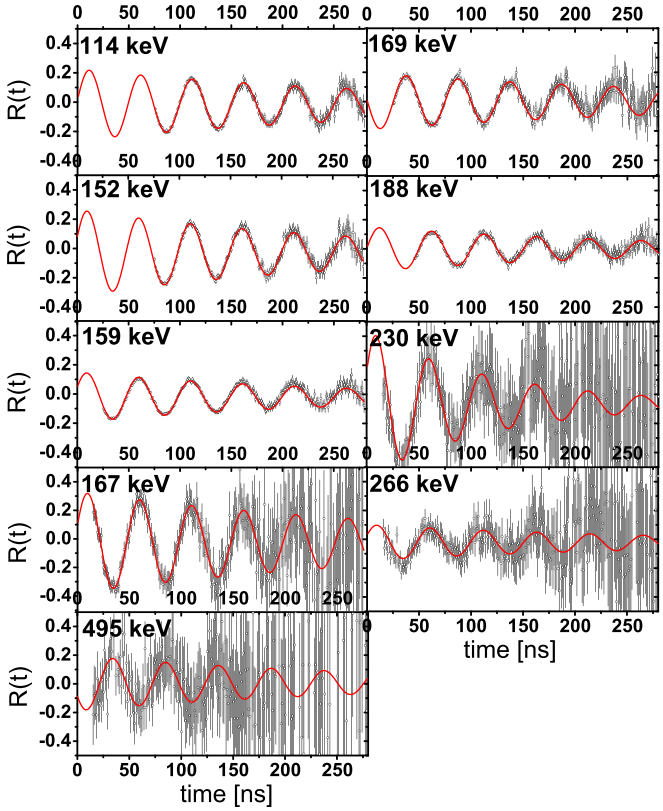

FIG. 7. Observed oscillating ratios $R(t)$

where an additional parameter, the phase ϕ, was introduced to account for possible timing offsets of the detectors. Figure 7 shows modulation spectra constructed by means of Eq. (2) with least-squares fits of formula (5) shown as solid lines. The approximate modulation formula describes the experimental data very well, indicating that the assumption of small A_4 coefficients and identical detectors is a sufficient approximation for the Larmor frequency to be measured. However, this approximation may not be correct for gamma angular distribution coefficients determination that may be sensitive to spectra normalization and summation.

One can see in Fig. 7 attenuated oscillation amplitudes, which may come from the hyperfine interaction between the nuclear magnetic moment of Cs recoils and the magnetic moments of the electronic shells in Sn target causing a spin deorientation effect. The relaxation time of the spin deorientation and the corresponding oscillation attenuation is around $\tau_{\rm rel} \approx 300$ ns. The deorientation effect was included in the fitted formula by the spin alignment coefficients $\alpha(t)$ taken as an exponential function of time, $\alpha_2(t) = \alpha_2 \exp(-t/\tau_{\rm rel})$. Thus the final approximate function for the observed modulation ratio becomes

$$R(t) \approx \frac{-3\exp(-t/\tau_{\rm rel})A\sin(2\omega_L t - \phi)}{4 + A\exp(-t/\tau_{\rm rel})}, \qquad (6)$$

where $A = \alpha_2 Q_2 A_2$ was assigned as the value related to the initial modulation amplitude.

All excited states above the isomer belong to collective bands with picosecond lifetimes [3] so they do not contribute to the modulation of the intensity ratio $R(t)$. This is particularly important information, since the experiment discussed here is a γ-distribution measurement and not the γ-correlation measurement. The oscillation frequency observed in all transitions can therefore be attributed to the g factor of the $I = 9^+$ band.

TABLE I. Parameters of the oscillation function given by Eq. (6) resulting from the fitting procedure.

E_γ (keV)	A	ω_L (10^9 s^{-1})	ϕ (deg)	$\tau_{\rm rel}$ (ns)
114	−0.243(9)	0.0625(1)	7.9 ± 2.0	334 ± 34
152	−0.296(4)	0.0622(1)	19.7 ± 0.7	279 ± 12
159	−0.172(3)	0.0620(1)	23.6 ± 1.0	255 ± 15
167	−0.35(2)	0.0618(4)	20.7 ± 3.4	360 ± 101
169	+0.193(6)	0.0631(2)	−3.7 ± 1.6	373 ± 53
188	−0.153(7)	0.0625(2)	3.3 ± 2.5	277 ± 36
230	−0.51(7)	0.062(1)	25.6 ± 9.5	123 ± 31
266	−0.12(1)	0.061(2)	24.2 ± 14.7	300[a]
495	+0.19(3)	0.062(2)	28.1 ± 23.3	300[a]

[a]Fixed during fitting.

The A, $\tau_{\rm rel}$, ω_L, and ϕ parameters were kept free for the least-squares fits of the formula (6), giving the results listed in Table I. One can see that the Larmor frequency ω_L in all of the oscillation functions is nearly the same (Table I, column 3). This suggests that the intensity ratio $R(t)$ comes from fast (compared to the studied magnetic moment precession period) γ transitions below the $I = 9^+$ isomer.

Individual properties of excited states below the isomer, i.e., their lifetimes (on the order of a few nanoseconds) and the values and signs of their g factors, may influence the value of the phase ϕ. Short-term precession of the magnetic moment in each of these states may slightly increase or decrease (depending on the sign of the g factor) the value of the phase ϕ. This fact may explain the differences in the values of the phase observed in the presented measurement (see Table I, column 4).

The average value of the Larmor frequency $\omega_L = 0.0621(4) \times 10^9$ s^{-1} leads to precise value of the g factor $g = 0.59(1)$ and the deorientation relaxation time $\tau = 3.43(8) \times 10^{-7}$ s [8], which are the final experimental results. The obtained g-factor value is about 20% larger than that expected theoretically in frame of core particle hole coupling (CPHC) calculations with γ-rigid as well as γ-soft core [10,11].

IV. $\pi h_{11/2} \otimes \nu h_{11/2}^{-1}$ $I = 9^+$ BANDHEAD CONFIGURATION

The measured value of the g factor for the $I = 9^+$ bandhead allows to verify whether the total angular momentum vector of the 9^+ bandhead is built chiefly by the two angular momentum vectors of the odd $\pi h_{11/2} \otimes \nu h_{11/2}^{-1}$ nucleons or a third component coming from significant even-even core rotation is required to reproduce the value observed experimentally.

In case where only two angular momentum vectors of the two odd nucleons contribute to the total spin of the isomeric state (no core rotation), there is only one coupling scheme giving the required total angular momentum $J = 9\hbar$. The g factor of such a two-component state can be calculated using

TABLE II. Estimation of the g-factor value of $I = 9^+$ in ^{128}Cs based on pure theoretical calculations (first raw) and on experimental data taken from neighboring nuclei (second and third raw) with comparison to the experimentally obtained g factor. Column 1: Orbitals from which the input values are taken. Column 2: Isotopes from which the input data are taken. Columns 3 and 4: Values of single-particle proton and neutron g factors as the input data [12]. Columns 5 and 6: Values of spin gyromagnetic factors of proton and neutron calculated from proton and neutron single-particle g factors. Columns 7 and 8: Single-particle g factors for proton and neutron expected in the $h_{11/2}$ orbital from corresponding spin gyromagnetic factors. Column 9: Values of the g factor in the $\pi h_{11/2} \otimes \nu^{-1} h_{11/2} I = 9^+$ state of ^{128}Cs expected for the two-component model (no core rotation). Column 10: Value of the g factor obtained experimentally.

Orbital	Isotope	g^j proton	g^j neutron	g^s proton	g^s neutron	g_p	g_n	g	$g_{\text{experiment}}$
$h_{11/2}$ theoretical	^{128}Cs	1.21	−0.21	3.31	−2.31	1.21[a]	−0.21[a]	0.50[a]	0.59(1) (experimental)
$h_{11/2}$	^{129}Cs(proton)/ ^{129}Xe(neutron)	1.191(18)	−0.1619(2)	3.10(2)	−1.781(2)	1.191(18)	−0.1619(2)	0.515(9)	
$s_{1/2}$	^{127}Cs(proton)/ ^{129}Xe(neutron)	2.98(2)	−1.555953(15)	2.98(2)	−1.555953(15)	1.1802(15)	−0.1414502(15)	0.519(2)	

[a]Gyromagnetic factors of proton g_p and neutron g_n estimated from the free-particle values using the attenuation factor 0.6 for the nucleon spin gyromagnetic factors.

the additivity formula [13]

$$g = \frac{1}{2J(J+1)}\{g_p[J(J+1) + j_p(j_p+1) - j_n(j_n+1)] + g_n[J(J+1) - j_p(j_p+1) + j_n(j_n+1)]\}, \quad (7)$$

where g_p and g_n are g factors of the odd proton and odd neutron, respectively.

For the $\pi h_{11/2} \otimes \nu h_{11/2}^{-1}$ configuration, the angular momentm of the proton, j_p, and the neutron, j_n, equals $11/2\hbar$ and the above formula simplifies to

$$g = \tfrac{1}{2}(g_p + g_n). \quad (8)$$

To find the values of g_p and g_n one can use theoretical estimations [14–16] or adopt them from experimental data of magnetic moments measured in the neighboring single-odd nuclei. For a single nucleon occupying the $j = l \pm s$ orbital, its g-factor value can be written as

$$g^j = \frac{(2j-1)g^l + g^s}{2j} \quad \text{for} \quad j = l + \frac{1}{2}, \quad (9)$$

$$g^j = \frac{(2j+3)g^l - g^s}{2(j+1)} \quad \text{for} \quad j = l - \frac{1}{2}. \quad (10)$$

These two equations allow one to express the g_p and g_n values for any nuclear orbital provided that the spin-gyromagnetic factors g^s of these particles are known, or conversely, for the known g-factor value of a specified orbital it is possible to get the g^s values. By taking the orbital gyromagnetic factor $g^l = 1$ for the proton and $g^l = 0$ for the neutron together with the measured magnetic moments of states in neighboring nuclei, one can get an estimation of the associated g^s values.

^{128}Cs is a doubly-odd nucleus with 73 neutrons and 55 protons. In a single-odd neighbors, one can get either the features of the proton states from ^{129}Cs data (74 neutrons, 55 protons) or the features of the neutron states from ^{129}Xe data (75 neutrons, 54 protons). In both neighboring nuclei, the magnetic moments (that is the g factors) in the $h_{11/2}$ as well as $s_{1/2}$ states have been measured [17]. The measured magnetic moments of these specified states allow, by using Eq. (9), getting the experimental values of the spin gyromagnetic factor g^s associated with odd proton and odd neutron. The obtained theoretical and experimental g^s values for proton and neutron are summarized in Table II and are used in further calculations for other orbitals. The g^s values listed in Table II were used to calculate g_p and g_n values for particle configurations possibly involved in the structure of the $I = 9^+$ isomeric state. The obtained g_p and g_n values were then used to calculate the expected g factor of the isomeric bandhead for the $\pi h_{11/2} \otimes \nu h_{11/2}^{-1}$ configuration; see Eq.(8). All those values are listed in Table II.

By taking the g_p and g_n from theoretical estimates for $h_{11/2}$ orbitals in ^{128}Cs, one gets a purely theoretical expectation of the g-factor value for the $I = 9^+$ isomeric state. Another possibility is to take the g_p and g_n values from magnetic moments measured for $h_{11/2}$ states in single-odd neighbors. Since the same orbitals are involved in $\pi h_{11/2} \otimes \nu h_{11/2}^{-1}$ chiral configuration in ^{128}Cs, the expected g-factor value should have the best correspondence to $g = 0.59(1)$ reported here. Finally, one can use the experimental g-factor values available for $s_{1/2}$ states in single-odd neighbors that, according to Eq. (9), are equivalent to spin-gyromagnetic factors g_s of the odd proton and of the odd neutron. These spin-gyromagnetic factors together with Eqs. (9) and (10) give the single-particle g_p and g_n values for the $h_{11/2}$ orbital needed to obtain the g-factor value of the isomeric state. The three discussed scenarios give three expectation values of the g factor around 0.51 for each tested particle configuration within the simplest two-component model where the core rotation is excluded.

The discrepancy of the g-factor value $g = 0.51$ expected theoretically and the experimental value $g = 0.59(1)$, see Table II, shows that the total spin of the $I = 9^+$ isomeric state cannot be built chiefly by two angular momentum vectors of the odd nucleons. A significant core rotation component needs to be present in order to drive the g factor from $g = 0.51$ towards the experimental value $g = 0.59(1)$. Thus, in the following we introduce a three-component model which is appropriate for chiral geometry analysis.

V. CHIRAL GEOMETRY IN A THREE-COMPONENT MODEL OF THE *g* FACTOR

In the chiral scenario the odd-odd ^{128}Cs nucleus studied here is built of three components contributing to the total magnetic moment of the isomeric state: the even-even core, the odd proton, and the odd neutron with angular momentum vectors $\mathbf{j}_R$, $\mathbf{j}_p$, and $\mathbf{j}_n$ respectively.

For the sake of simplicity, we calculate first the *g*-factor value using an additivity formula for the nuclear magnetic moment generalized to the three-component system. In such a system, the total angular momentum vector of an excited state $\mathbf{J}$ is a sum of angular momentum vectors of the components, which in the case of the ^{128}Cs nucleus are the angular momenta of odd proton $\mathbf{j}_p$, odd neutron hole $\mathbf{j}_n$, and even-even core $\mathbf{j}_R$,

$$\mathbf{j}_p + \mathbf{j}_n + \mathbf{j}_R = \mathbf{J}. \tag{11}$$

Thus the magnetic moment of a three-component system becomes

$$\begin{aligned}\mu &= gJ\mu_N = \langle JJ|gJ_z|JJ\rangle\mu_N \\ &= \langle JJ|g_p j_{pz} + g_n J_{nz} + g_R J_{Rz}|JJ\rangle\mu_N,\end{aligned} \tag{12}$$

where J_z, j_{pz}, j_{nz}, and j_{Rz} are the angular momentum projection operators on the quantization axis of the total spin and the spins of the proton, neutron, and core, respectively. With the use of the generalized Landé formula [13], the above equation can be expressed by the scalar product operators $\mathbf{j}_p \cdot \mathbf{J}$, $\mathbf{j}_n \cdot \mathbf{J}$, and $\mathbf{j}_R \cdot \mathbf{J}$,

$$\begin{aligned}\mu = &\frac{\langle JJ|g_p\mathbf{j}_p \cdot \mathbf{J} + g_n\mathbf{j}_n \cdot \mathbf{J} + g_R\mathbf{j}_R \cdot \mathbf{J}|JJ\rangle}{J(J+1)} \\ &\times \langle JJ|J_z|JJ\rangle\mu_N.\end{aligned} \tag{13}$$

The *g* factor is thus given by the formula

$$g = \frac{\langle JJ|g_p\mathbf{j}_p \cdot \mathbf{J} + g_n\mathbf{j}_n \cdot \mathbf{J} + g_R\mathbf{j}_R \cdot \mathbf{J}|JJ\rangle}{J(J+1)}. \tag{14}$$

By using the relation

$$J^2 = j_p^2 + j_n^2 + j_R^2 + 2\mathbf{j}_p \cdot \mathbf{j}_n + 2\mathbf{j}_p \cdot \mathbf{j}_R + 2\mathbf{j}_n \cdot \mathbf{j}_R, \tag{15}$$

one can write the final form of the *g*-factor expression, where only the scalar product operators of components are used,

$$\begin{aligned}g = &\frac{1}{2}(g_p + g_n + g_R) \\ &+ \frac{1}{J(J+1)}\frac{1}{2}j_p(j_p+1)(g_p - g_n - g_R) \\ &+ \frac{1}{J(J+1)}\frac{1}{2}j_n(j_n+1)(g_n - g_p - g_R) \\ &+ \frac{1}{J(J+1)}\frac{1}{2}j_R(j_R+1)(g_R - g_p - g_n) \\ &- \frac{1}{J(J+1)}(g_p\langle\mathbf{j}_n \cdot \mathbf{j}_R\rangle + g_n\langle\mathbf{j}_p \cdot \mathbf{j}_R\rangle + g_R\langle\mathbf{j}_p \cdot \mathbf{j}_n\rangle).\end{aligned} \tag{16}$$

Comparing the above generalized equation with the one derived from the coupling of only two angular momentum vectors [the additivity formula (7)], one can see that, apart from the combinations of j_p^2, j_n^2, and j_R^2 quantities related to lengths of angular momentum vectors, an additional part that contains scalar products of the angular momentum vector pairs has appeared and thus is sensitive to their mutual orientation. The occurrence of this part has a geometrical physical explanation.

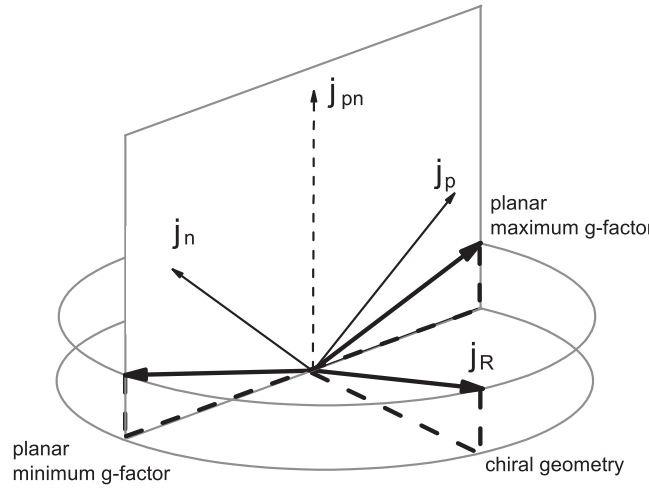

FIG. 8. Core angular momentum $\mathbf{j}_R$ may be coupled at different precession angles about the resultant $\mathbf{j}_{pn}$ of proton and neutron angular momentum to form the specified spin of the isomeric state. The planar geometry where $\mathbf{j}_R$ tends toward $\mathbf{j}_p$ gives the highest possible value of the *g* factor. The second planar geometry where $\mathbf{j}_R$ tends toward $\mathbf{j}_n$ gives the lowest possible value of the *g* factor. Aplanar geometry corresponding to chiral configuration gives the *g*-factor value in between.

In case of the coupling of only two angular momentum vectors, the value of the total spin determines unambiguously their mutual orientation and the resulting magnetic moment. This does not hold for the coupling of three angular momentum vectors, where the same value of the total spin *J* can be attained at different angles between each pair of them, giving different *g* factors. The last part of Eq. (16) vanishes for the ideal chiral geometry with all the vectors being mutually perpendicular, therefore the first four parts correspond to the *g*-factor value with maximum chirality g_{chiral} and Eq. (16) takes the simple form

$$g = g_{\text{chiral}} - \frac{1}{J(J+1)}(g_p\langle\mathbf{j}_n \cdot \mathbf{j}_R\rangle + g_n\langle\mathbf{j}_p \cdot \mathbf{j}_R\rangle + g_R\langle\mathbf{j}_p \cdot \mathbf{j}_n\rangle). \tag{17}$$

Semiclassical sequential coupling of the three angular momentum vectors explains the dependence of the *g*-factor value on their mutual angles.

Figure 8 shows the angular momentum of the proton j_p and of the neutron j_n coupled to their resultant spin j_{pn}. The angular momentum of the core j_R may then be coupled to j_{pn} at various precession angles to get the desired total spin *J*. In general, there are three characteristic cases given by this precession degree of freedom. The first case is the maximum aplanarity of the three angular momentum vectors, where the j_R vector goes as far as possible off the plane spanned by j_p and j_n, giving a *g*-factor value corresponding

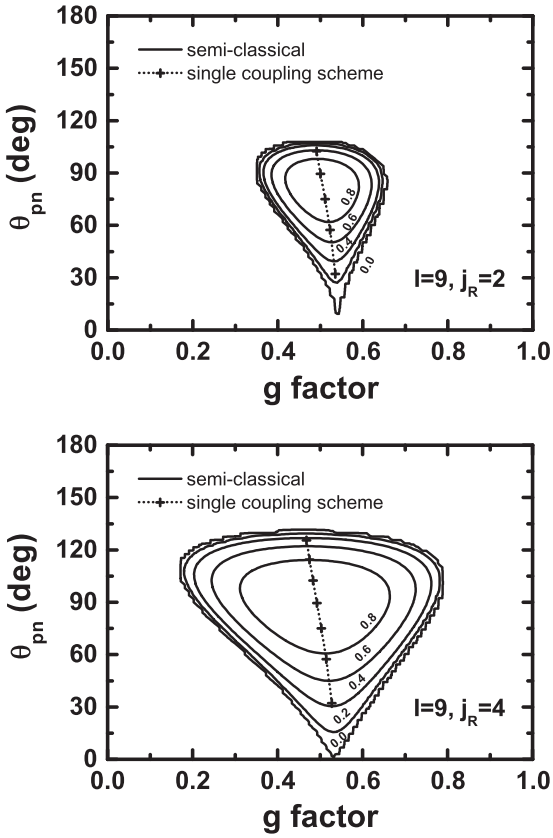

FIG. 9. The g-factor value expected for coupling of $\pi h_{11/2} \otimes \nu h_{11/2}^{-1}$ and core angular momenta $j_R = 2\hbar$ (upper panel) and $j_R = 4\hbar$ (lower panel) to the total spin $I = 9\hbar$ of the isomeric state. Experimental values of g_p and g_n estimated from the $h_{11/2}$ orbital in single-odd neighboring nuclei were used.

to the maximum chirality. In the ideal chiral geometry, the g factor takes the value g_{chiral}. The next characteristic case is the planar geometry, where the angle between j_R and j_p attains a minimum value while the angle between j_R and j_n is the highest. Then, the scalar product $\mathbf{j}_p \cdot \mathbf{j}_R$ has its maximum and the $\mathbf{j}_n \cdot \mathbf{j}_R$ product its minimum. These scalar products are multiplied in Eq. (16) by g_n and g_p factors of opposite sign. Thus, in this scenario the part sensitive to the orientation of the three angular momentum vectors becomes maximally positive, giving the highest g-factor value. The last characteristic case is an opposite planar geometry where j_R and j_n vectors become closest and the angle between j_R and j_p is highest, leading to the maximum negative value of the part sensitive to angular momentum vector geometry in Eq. (16). Such a geometry leads to the lowest value of the g factor. The two planar cases determine the limits of possible g-factor values for a given j_p and j_n coupling.

By making a plot of possible g-factor values versus the angle between proton and neutron angular momentum vectors one gets a droplike shape containing all possible coupling schemes of the three components j_p, j_n, and j_R to the total spin J. Figure 9 shows two such plots for the coupling of $\pi h_{11/2} \otimes \nu h_{11/2}^{-1}$ configuration with two main non-zero core angular momentum values $j_R = 2\hbar$ and $j_R = 4\hbar$ to the total spin $I = 9\hbar$ of the isomeric state. Contours shown in the plots present the absolute value of the normalized orientation parameter [18]

$$o = \frac{(\mathbf{j}_p \times \mathbf{j}_n) \cdot \mathbf{j}_R}{|\mathbf{j}_p||\mathbf{j}_n||\mathbf{j}_R|}, \tag{18}$$

calculated for each coupling scheme inside of the droplike shape. The values of this parameter which are close to the zero correspond to planar $|P\rangle$ configuration where all three angular momenta are in one plane. One can see that the planar configuration gives the outer border of the plot. Conversely, the values located in the middle of the plot which are close to unity correspond to the ideal chiral configurations $|L\rangle$ and $|R\rangle$, where the three spins are perpendicular to each other.

According to Ref. [19], the existence of the chiral critical frequency would result in the planar orientation of the three angular momentum vectors for the $I = 9\hbar$ isomeric bandhead. From the two opposite planar geometries, the one with proton angular momentum j_p tending towards the momentum of the core j_R is energy favored by Coriolis interaction. Therefore, the expected planar geometry should have the highest g-factor value for a given angle θ_{pn} between j_p and j_n. This may lead to the g-factor values $g \approx 0.5$, $g \approx 0.65$, and $g \approx 0.8$ for the proton and the neutron coupled to the core state with $j_R = 0\hbar$ (two-component model), $j_R = 2\hbar$, and $j_R = 4\hbar$ (three-component model), respectively. The wave function of the isomeric state is a composition of several core rotational states. Contributions of $j_R = 2\hbar$, $j_R = 4\hbar$, and higher (not discussed here) core rotations may drive the g factor from $g = 0.51$ expected for $j_R = 0\hbar$ to the experimental value $g = 0.59(1)$ provided there is planar geometry in the isomeric bandhead.

The above analysis shows that the two-component model where the total spin of the isomeric state is built chiefly by the angular momentum vectors of the two odd nucleons cannot reproduce the experimental g-factor value. The composition of the wave function with the nonzero core rotation (the three-component model) is needed to reproduce the measured g factor within the pure $\pi h_{11/2} \otimes \nu h_{11/2}^{-1}$ configuration, where a nonchiral geometry of the isomeric bandhead is expected. The wave function composition is discussed in a quantum-mechanical approach in the following sections.

VI. QUANTUM MECHANICAL CALCULATION OF THE *g* FACTOR OF A THREE-BODY SYSTEM

In the semiclassical models discussed above, the angular momentum vectors $\mathbf{j}$ were taken as classical vectors with three spatial components well defined and the length $j(j+1)$. Except for triangularity, these models do not impose any condition on the mutual angles between these three coupled vectors. In general, the idea of nuclear chirality requires that all three spatial components of the coupled spins be well defined, which seems to contradict the quantum approach, where only the length and the projection on the quantization axis are defined for an angular momentum vector. It is therefore essential to begin with principles of the chiral geometry emerging in quantum systems.

The nuclear state of a definite spin, $|JM\rangle$, can be expressed as a product of the states of proton $|j_p\rangle$, neutron $|j_n\rangle$, and core $|j_R\rangle$ coupled to the total angular momentum as follows: $\mathbf{j}_p$, $\mathbf{j}_n$ coupled to a vector $\mathbf{j}_{pn} = \mathbf{j}_p + \mathbf{j}_n$, which, in turn, is coupled with $\mathbf{j}_R$ to $\mathbf{J} = \mathbf{j}_{pn} + \mathbf{j}_R$,

$$|(j_p j_n) j_{pn} j_R; JM\rangle = \sum_{m_p, m_n, m_{pn}, m_R} \langle j_p m_p j_n m_n | j_{pn} m_{pn}\rangle \langle j_{pn} m_{pn} j_R m_R | JM\rangle |j_p m_p\rangle |j_n m_n\rangle |j_R m_R\rangle. \tag{19}$$

There are several possible j_{pn} quantum numbers, indicating that the total spin state $|JM\rangle$ may be formed in several ways, here called coupling schemes. A single coupling scheme given by Eq. (19) defines a unique set of expected mutual angles between each pair of the angular momentum vectors. For the total spin state $|JM\rangle$ resulting from a single coupling scheme, its g factor can be calculated analytically using angular momentum algebra. The matrix elements of the squares and scalar products in Eq. (16) for a single coupling scheme are given by

$$\langle (j_p' j_n') j_{pn}' j_R'; J'M' | \mathbf{j}_p^2 | (j_p j_n) j_{pn} j_R; JM\rangle = \delta_{J'J}\delta_{M'M}\delta_{j_p' j_p}\delta_{j_n' j_n}\delta_{j_R' j_R}\delta_{j_{pn}' j_{pn}} j_p(j_p+1), \tag{20}$$

$$\langle (j_p' j_n') j_{pn}' j_R'; J'M' | \mathbf{j}_n^2 | (j_p j_n) j_{pn} j_R; JM\rangle = \delta_{J'J}\delta_{M'M}\delta_{j_p' j_p}\delta_{j_n' j_n}\delta_{j_R' j_R}\delta_{j_{pn}' j_{pn}} j_n(j_n+1), \tag{21}$$

$$\langle (j_p' j_n') j_{pn}' j_R'; J'M' | \mathbf{j}_R^2 | (j_p j_n) j_{pn} j_R; JM\rangle = \delta_{J'J}\delta_{M'M}\delta_{j_p' j_p}\delta_{j_n' j_n}\delta_{j_R' j_R}\delta_{j_{pn}' j_{pn}} j_R(j_R+1), \tag{22}$$

$$\begin{aligned}\langle (j_p' j_n') j_{pn}' j_R'; J'M' | \mathbf{j}_p \cdot \mathbf{j}_n | (j_p j_n) j_{pn} j_R; JM\rangle &= \delta_{J'J}\delta_{M'M}\delta_{j_p' j_p}\delta_{j_n' j_n}\delta_{j_R' j_R}\delta_{j_{pn}' j_{pn}} (-1)^{j_p + j_n + j_{pn}} \\ &\times \sqrt{j_p(j_p+1)(2j_p+1) j_n(j_n+1)(2j_n+1)} \begin{Bmatrix} j_p & j_n & j_{pn} \\ j_n & j_p & 1 \end{Bmatrix},\end{aligned} \tag{23}$$

$$\begin{aligned}&\langle (j_p' j_n') j_{pn}' j_R'; J'M' | \mathbf{j}_p \cdot \mathbf{j}_R | (j_p j_n) j_{pn} j_R; JM\rangle \\ &= \delta_{J'J}\delta_{M'M}\delta_{j_p' j_p}\delta_{j_n' j_n}\delta_{j_R' j_R} (-1)^{j_R + j_p + j_n + J + 1} \\ &\times \sqrt{(2j_{pn}+1)(2j_{pn}'+1)} \sqrt{j_p(j_p+1)(2j_p+1)} \sqrt{j_R(j_R+1)(2j_R+1)} \begin{Bmatrix} j_p & j_{pn} & j_n \\ j_{pn}' & j_p & 1 \end{Bmatrix} \begin{Bmatrix} j_{pn} & j_R & J \\ j_R & j_{pn}' & 1 \end{Bmatrix},\end{aligned} \tag{24}$$

$$\begin{aligned}&\langle (j_p' j_n') j_{pn}' j_R'; J'M' | \mathbf{j}_n \cdot \mathbf{j}_R | (j_p j_n) j_{pn} j_R; JM\rangle \\ &= \delta_{J'J}\delta_{M'M}\delta_{j_p' j_p}\delta_{j_n' j_n}\delta_{j_R' j_R} (-1)^{j_R + j_p + j_n + J + 1 + j_{pn} + j_{pn}'} \\ &\times \sqrt{(2j_{pn}+1)(2j_{pn}'+1)} \sqrt{j_n(j_n+1)(2j_n+1)} \sqrt{j_R(j_R+1)(2j_R+1)} \begin{Bmatrix} j_n & j_{pn} & j_p \\ j_{pn}' & j_n & 1 \end{Bmatrix} \begin{Bmatrix} j_{pn} & j_R & J \\ j_R & j_{pn}' & 1 \end{Bmatrix},\end{aligned} \tag{25}$$

where nonzero values of the six-j symbols give all possible coupling schemes. One can calculate the set of the g-factor values corresponding to possible coupling schemes by substituting the matrix elements (20)–(25) together with the values of g_p, g_n, and g_R into Eq. (16). Two such sets, one for $j_R = 2\hbar$ and one for $j_R = 4\hbar$, are presented in Fig. 9 as small crosses connected with dotted lines. This analytical approach shows that the idea of nuclear chirality, with three well defined angles between the pairs of three spins, does not contradict the quantum angular momentum algebra.

In general, the state with definite spin $|JM\rangle$ is a superposition of many coupling schemes (below only the angular momentum quantum numbers are shown)

$$|JM\rangle = \sum_{j_p, j_n, j_{pn}, j_R} c_J(j_p, j_n, j_{pn}, j_R) |(j_p j_n) j_{pn} j_R; JM\rangle. \tag{26}$$

Then, the geometry defined by the mean values of the squares and scalar products of the three angular momentum vectors is also given by the superposition coefficients $c_J(j_p, j_n, j_{pn}, j_R)$. Indeed, the expectation values in question take for the wave packet the forms

$$\langle JM | \mathbf{j}_p^2 | JM\rangle = \sum_{j_p, j_n, j_{pn}, j_R} |c_J(j_p, j_n, j_{pn}, j_R)|^2 j_p(j_p+1), \tag{27}$$

$$\langle JM | \mathbf{j}_n^2 | JM\rangle = \sum_{j_p, j_n, j_{pn}, j_R} |c_J(j_p, j_n, j_{pn}, j_R)|^2 j_n(j_n+1), \tag{28}$$

$$\langle JM | \mathbf{j}_R^2 | JM\rangle = \sum_{j_p, j_n, j_{pn}, j_R} |c_J(j_p, j_n, j_{pn}, j_R)|^2 j_R(j_R+1), \tag{29}$$

$$\langle JM | \mathbf{j}_p \cdot \mathbf{j}_n | JM\rangle = \sum_{j_p, j_n, j_{pn}, j_R} |c_J(j_p, j_n, j_{pn}, j_R)|^2 \langle (j_p j_n) j_{pn} j_R; JM | \mathbf{j}_p \cdot \mathbf{j}_n | (j_p j_n) j_{pn} j_R; JM\rangle, \tag{30}$$

$$\langle JM|\mathbf{j}_p \cdot \mathbf{j}_R|JM\rangle = \sum_{j_p, j_n, j_{pn} j'_{pn}, j_R} c^*_J(j_p, j_n, j'_{pn}, j_R) c_J(j_p, j_n, j_{pn}, j_R) \langle (j_p j_n) j'_{pn} j_R; JM|\mathbf{j}_p \cdot \mathbf{j}_R|(j_p j_n) j_{pn} j_R; JM\rangle, \tag{31}$$

$$\langle JM|\mathbf{j}_n \cdot \mathbf{j}_R|JM\rangle = \sum_{j_p, j_n, j_{pn} j'_{pn}, j_R} c^*_J(j_p, j_n, j'_{pn}, j_R) c_J(j_p, j_n, j_{pn}, j_R) \langle (j_p j_n) j'_{pn} j_R; JM|\mathbf{j}_n \cdot \mathbf{j}_R|(j_p j_n) j_{pn} j_R; JM\rangle. \tag{32}$$

Such superpositions can be analyzed with available nuclear models which give the superposition coefficients $c_J(j_p, j_n, j_{pn}, j_R)$.

VII. PARTICLE ROTOR MODEL CALCULATIONS

In the present section, the g factor is calculated in the framework of the triaxial particle rotor model (PRM), whose formalism in detail can be found in Refs. [1,20–27].

In the present work, a many-particle–many-hole PRM [22,23] is used. The total Hamiltonian of PRM is expressed as

$$\hat{H}_{\rm PRM} = \hat{H}_{\rm coll} + \hat{H}_{\rm intr}, \tag{33}$$

with the collective rotor Hamiltonian

$$\hat{H}_{\rm coll} = \sum_{k=1}^{3} \frac{\hat{j}^2_{Rk}}{2\mathcal{J}_k} = \sum_{k=1}^{3} \frac{(\hat{J}_k - \hat{j}_{pk} - \hat{j}_{nk})^2}{2\mathcal{J}_k}, \tag{34}$$

where the indices $k = 1$, 2, and 3 refer to the three principal axes of the body-fixed frame. The $\hat{j}_{Rk}$ and $\hat{J}_k$ denote the angular momentum operators of the core and of the total nucleus, respectively, and the $\hat{j}_{pk}$ and $\hat{j}_{nk}$ the angular momentum operator of the valence protons and neutrons. Moments of inertia of the irrotational flow type are adopted, i.e., $\mathcal{J}_k = \mathcal{J}_0 \sin^2(\gamma - 2k\pi/3)$, with γ the triaxial deformation parameter. In addition, the intrinsic Hamiltonian is written as

$$H_{\rm intr} = \sum_{i=p,n} \sum_{\nu} \varepsilon_{i,\nu} a^\dagger_{i,\nu} a_{i,\nu}, \tag{35}$$

where $\varepsilon_{p,\nu}$ and $\varepsilon_{n,\nu}$ are the single-particle energies provided by the single-j shell

$$h_{\rm sp} = \pm\frac{1}{2} C \left\{ \cos\gamma \left(j_3^2 - \frac{j(j+1)}{3} \right) + \frac{\sin\gamma}{2\sqrt{3}} (j_+^2 + j_-^2) \right\}. \tag{36}$$

Here, the plus or minus sign refers to particle or hole, and the coefficient C is proportional to the quadrupole deformation β [28],

$$C = \left(\frac{123}{8} \sqrt{\frac{5}{\pi}} \right) \frac{2N+3}{j(j+1)} A^{-1/3} \beta. \tag{37}$$

The single-particle state and its time reversal state are expressed as

$$a^\dagger_\nu|0\rangle = \sum_{\alpha\Omega} c^\nu_{\alpha\Omega} |\alpha, j\Omega\rangle, \tag{38}$$

$$a^\dagger_{\bar{\nu}}|0\rangle = \sum_{\alpha\Omega} (-1)^{j-\Omega} c^\nu_{\alpha\Omega} |\alpha, j-\Omega\rangle, \tag{39}$$

where Ω is the projection of the single-particle angular momentum j along the three-axis of the intrinsic frame and is restricted to $\ldots, -3/2, 1/2, 5/2, \ldots$ due to the time-reversal degeneracy, and α denotes the other quantum numbers. For a system with $\sum_{i=p,n} N_i$ valence nucleons (N_i denotes the number of the protons or neutrons in the valence shell), the intrinsic wave function is given as

$$|\varphi\rangle = \prod_{i=p,n} \left(\prod_{l=1}^{n_i} a^\dagger_{i,\nu_l} \right) \left(\prod_{l=1}^{n'_i} a^\dagger_{i,\bar{\mu}_l} \right) |0\rangle, \tag{40}$$

with $n_i + n'_i = N_i$ and $0 \leqslant n_i \leqslant N_i$.

The total wave function can be expanded into the strong coupling basis

$$|JM\rangle = \sum_{K\varphi} c_{K\varphi} |JMK\varphi\rangle, \tag{41}$$

with

$$|JMK\varphi\rangle = \frac{1}{\sqrt{2(1+\delta_{K0}\delta_{\varphi,\bar{\varphi}})}} [|JMK\rangle|\varphi\rangle + (-1)^{I-K}|JM-K\rangle|\bar{\varphi}\rangle], \tag{42}$$

where $|JMK\rangle$ is the Wigner function $\sqrt{\frac{2J+1}{8\pi^2}} D^J_{MK}$. The basis states are symmetrized under the point group D_2, which leads to $K - \frac{1}{2}\sum_{i=1}^{4}(n_i - n'_i)$ being an even integer.

After obtaining the wave functions of PRM, the reduced transition probabilities $B(M1)$ and $B(E2)$ and the expectation values of the angular momentum of the system can be calculated [22,23]. For the g-factor calculation, one uses Eq. (14) [8,25,26].

In the PRM calculation, the configuration $\pi h_{11/2} \otimes \nu h^{-5}_{11/2}$ with the corresponding deformation parameters $\beta = 0.23$ and $\gamma = 24^\circ$, according to the adiabatic and configuration-fixed constrained covariant density functional theory (CDFT) calculations [8,29], are used with the PC-PK1 density functional [30]. The moment of inertia $\mathcal{J}_0 = 20\ \hbar^2/\text{MeV}$ is adjusted to fit the energy spectra of the yrast band. For the electromagnetic transitions, the empirical intrinsic quadrupole moment $Q_0 = (3/\sqrt{5\pi}) R_0^2 Z\beta$, and the g factors of proton g_p and neutron g_n given in Table II (see footnote [a] there) were adopted along with the core g-factor value $g_R = 0.41$ taken from ^{128}Xe 2^+ experimental data [31].

In Fig. 10, the energy spectra, the intraband $B(E2)$ and $B(M1)$, and the interband $B(M1)$ of the doublet bands in ^{128}Cs calculated by PRM in comparison with the experimental data available [3] are shown. The observed energy spectra are reproduced well, as shown in Fig. 10(a), including the energy difference between the partner bands. The trend of the calculated $B(E2)$ results deviates from the data due to the frozen nuclear shape. The staggering of the intraband and the interband $B(M1)$ can be seen in both the data and the calculated results, as shown in Figs. 10(c) and 10(d). Their strengths are reproduced reasonably. All of these agreements

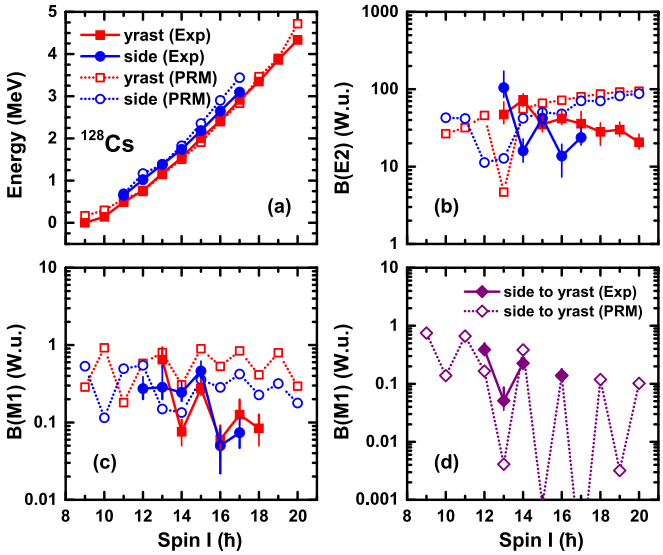

FIG. 10. (a) The energy spectra, (b) the intraband $B(E2)$, (c) the intraband $B(M1)$, and (d) the interband $B(M1)$ of the doublet bands in ^{128}Cs calculated by the PRM approach in comparison with the experimental data available [3].

support the correct assignment for the valence nucleon configuration.

The g factor is sensitive to the configuration and the triaxial deformation parameter. To further check the configuration assignment, we display in Fig. 11 the g-factor values for the 9^+ yrast bandhead as a function of triaxial deformation calculated by PRM with configurations $\pi h_{11/2} \otimes \nu h^{-5}_{11/2}$, $\pi h_{11/2} \otimes \nu h^{-3}_{11/2}$, and $\pi h_{11/2} \otimes \nu h^{-1}_{11/2}$. In these calculations, the triaxial deformation parameter is varied. For the neutron configuration, -5 denotes that there are five holes located in the $h_{11/2}$ shell and four of them are paired (occupying the time state and time-reversal state). One notices that if the triaxial deformation parameter is equal to that obtained from the

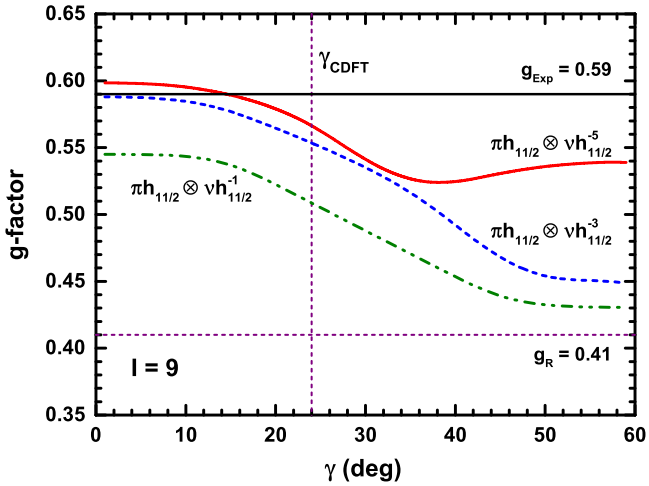

FIG. 11. The g-factor values for the 9^+ yrast bandhead as a function of triaxial deformation calculated by PRM with configurations $\pi h_{11/2} \otimes \nu h^{-5}_{11/2}$, $\pi h_{11/2} \otimes \nu h^{-3}_{11/2}$, and $\pi h_{11/2} \otimes \nu h^{-1}_{11/2}$.

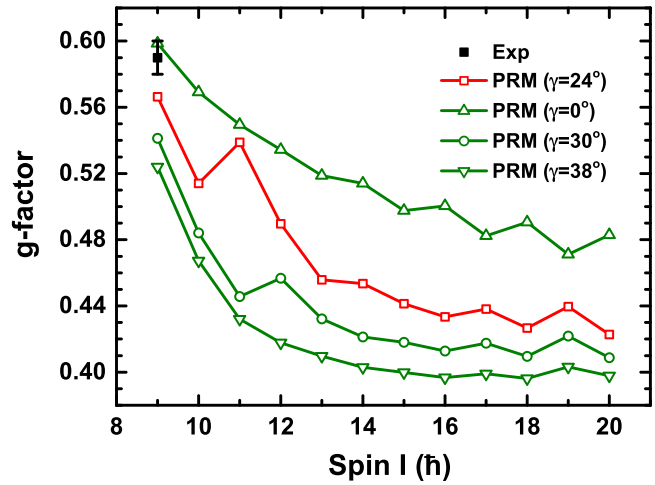

FIG. 12. The g-factor values as functions of spin expected for $\pi h_{11/2} \otimes \nu h^{-5}_{11/2}$ yrast band levels with triaxial deformation parameters $\gamma = 0^\circ$, 24°, 30°, and 38°.

constrained CDFT calculations, the calculated g factor with the configuration $\pi h_{11/2} \otimes \nu h^{-5}_{11/2}$, which is also predicted by the constrained CDFT calculations, is closest to the experimental value.

By keeping the quadrupole deformation and decreasing the parameter $\gamma \to 0^\circ$ the nuclear shape becomes axially symmetric with prolate deformation. This is the second characteristic case of the nuclear orientation as discussed above, i.e., planar geometry with the angle between j_R and j_p attaining a minimum value while the angle between j_R and j_n is the highest, and gives the highest g-factor value. The nonchiral g-factor values obtained with axially symmetric core for configurations $\pi h_{11/2} \otimes \nu h^{-5}_{11/2}$ ($g \approx 0.60$) and $\pi h_{11/2} \otimes \nu h^{-3}_{11/2}$ ($g \approx 0.59$) agree very well with the experimental g factor $g = 0.59(1)$. When increasing the parameter $\gamma \to 60^\circ$, the nuclear shape becomes oblately deformed. For the configurations $\pi h_{11/2} \otimes \nu h^{-3}_{11/2}$ and $\pi h_{11/2} \otimes \nu h^{-1}_{11/2}$, the neutron angular momentum j_n aligns mainly along the long axis and becomes close to the j_R, while the angle between j_R and j_p is highest. This is the third characteristic case of the nuclear orientation and leads to the lowest g-factor value. For the configuration $\pi h_{11/2} \otimes \nu h^{-5}_{11/2}$ with lower neutron Fermi surface, the situation become complicated. The lowest g-factor value does not appear at $\gamma \approx 60^\circ$, but $\gamma \approx 38^\circ$. This might be due to the fact that the neutron angular momentum has large intermediate axis component at $\gamma \approx 38^\circ$ and becomes close to the core angular momentum j_R.

Figure 12 presents g-factor values as functions of spin expected for $\pi h_{11/2} \otimes \nu h^{-5}_{11/2}$ yrast band levels with triaxial deformation parameters $\gamma = 0^\circ$ (axial symmetric limit), 24° (obtained from constrained CDFT), 30° (maximal asymmetric deformation), and 38° (gives lowest g-factor value at bandhead) in comparison with the available experimental data. For the triaxially deformed core $\gamma = 24^\circ$ the g-factor value $g = 0.57$ is obtained for the calculated 9^+ bandhead. This value decreases with spin and reaches $g \approx 0.42$ for spin $I = 20\hbar$.

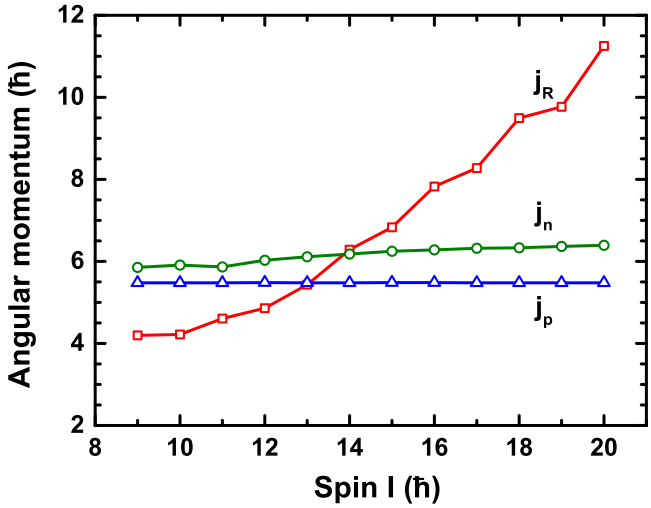

FIG. 13. The absolute values of angular momentum of proton j_p, neutron j_n, and core j_R as functions of spin expected for $\pi h_{11/2} \otimes \nu h_{11/2}^{-5}$ yrast band levels with triaxial deformation parameters $\gamma = 24^\circ$.

One can see in Fig. 12 that the g factors of the yrast states for the triaxial shapes of the nucleus are systematically smaller than the corresponding values for the axial deformation $\gamma = 0^\circ$. It indicates that the geometry of the three angular momentum vectors evolves from the planar limit toward the chiral one.

As mentioned above, a two-component model without including the core angular momentum contribution gives a large discrepancy in comparison with the experimental data. To check this in the framework of PRM, we plot in Fig. 13 the absolute values of angular momentum of core j_R together with proton j_p and neutron j_n as functions of spin for $\pi h_{11/2} \otimes \nu h_{11/2}^{-5}$ yrast band levels with the triaxial deformation parameter $\gamma = 24^\circ$. In the calculations, the angular momentum value j is determined by

$$j = \sqrt{\langle j_1^2 \rangle + \langle j_2^2 \rangle + \langle j_3^2 \rangle + 1/4} - 1/2. \tag{43}$$

Note that the proton angular momentum is a good quantum number, while the angular momenta of five neutron holes and core are not. One can see that j_n does not change much with increasing spin. However, j_R increases from $j_R \approx 4.2\hbar$ at $I = 9\hbar$ to $j_R \approx 11.3\hbar$ at $I = 20\hbar$, which indicates that the angular momentum of the rotor plays gradually more important roles than those of the proton particle and neutron holes. Thus, although the rotor angular momentum at the bandhead of ^{128}Cs yrast band is smaller than those of proton and neutron, it cannot be overlooked.

VIII. SUMMARY

Spontaneous chiral symmetry breaking in the ^{128}Cs nucleus was previously reported through observation of two nearly degenerated rotational bands with specific selection rules of the gamma transitions. These features were observed for significant nuclear rotation corresponding to $I > 13\hbar$ of the excited states. For lower spins the rotational band which is partner to the yrast band is not seen experimentally, suggesting the existence of the critical frequency of the chiral rotation. Below the critical frequency the chiral geometry of the three angular momentum vectors is prevented, possibly canceling the degeneration of the yrast and yrare bands. The hypothesis of the critical frequency was explored through g-factor measurement of the yrast bandhead within the TDAPD method. The experimental results were discussed in the frame of quantum angular momentum algebra and semiclassical calculations, and in the framework of PRM.

The experimental g-factor value of the isomeric $I = 9^+$ bandhead of the yrast states is well reproduced by PRM with the planar geometry of the three spins obtained in the limit of axially symmetric deformation. This result may explain the absence of the low spin yrare states and is the first indication of the existence of the chiral critical frequency.

ACKNOWLEDGMENTS

The authors wish to thank the ORSAY Tandem team for providing an excellent and stable beam. This project was supported in part by the Polish National Science Centre (NCN), Grant No 2013/10/M/ST2/00427. This work was partially supported by the Polish-French Collaboration COPIN-IN2P3 (06-121). This work was partly supported by the National Key R&D Program of China (Contracts No. 2018YFA0404400 and No. 2017YFE0116700) and the National Natural Science Foundation of China (Grants No. 12070131001, No. 11875075, No. 11935003, and No. 11975031).

[1] S. Frauendorf and J. Meng, Nucl. Phys. A **617**, 131 (1997).
[2] T. Koike, K. Starosta, C. J. Chiara, D. B. Fossan, and D. R. LaFosse, Phys. Rev. C **67**, 044319 (2003).
[3] E. Grodner, J. Srebrny, A.A. Pasternak, I. Zalewska, T. Morek, C. Droste, J. Mierzejewski, M. Kowalczyk, J. Kownacki, M. Kisieliński, S.G. Rohozinski, T. Koike, K. Starosta, A. Kordyasz, P.J. Napiorkowski, M. Wolinska-Cichocka, E. Ruchowska, W. Plociennik, and J. Perkowski, Phys. Rev. Lett. **97**, 172501 (2006).
[4] T. Koike, K. Starosta, and I. Hamamoto, Phys. Rev. Lett. **93**, 172502 (2004).
[5] E. Grodner, I. Sankowska, T. Morek, S. G. Rohoziński, C. Droste, J. Srebrny, A. A. Pasternak, M. Kisieliński, M. Kowalczyk, J. Kownacki *et al.*, Phys. Lett. B **703**, 46 (2011).
[6] T. Marchlewski, R. Szenborn, J. Samorajczyk, E. Grodner, J. Srebrny, C. Droste, L. Próchniak, A. A. Pasternak, M. Kowalczyk, M. Kisieliński *et al.*, Acta Phys. Pol. B **46**, 689 (2015).
[7] P. Olbratowski, J. Dobaczewski, and J. Dudek, Phys. Rev. C **73**, 054308 (2006).
[8] E. Grodner, J. Srebrny, C. Droste, L. Prochniak, S. G. Rohozinski, M. Kowalczyk, M. Ionescu-Bujor, C. A. Ur,

K. Starosta, T. Ahn, M. Kisielinski, T. Marchlewski, S. Aydin, F. Recchia, G. Georgiev, R. Lozeva, E. Fiori, M. Zielinska, Q. B. Chen, S. Q. Zhang, L. F. Yu, P. W. Zhao, J. Meng, Phys. Rev. Lett. **120**, 022502 (2018).

[9] E. Grodner *et al.* (unpublished).

[10] C. Droste, S. G. Rohoziński, K. Starosta, L. Próchniak, and E. Grodner, Eur. Phys. J. A **42**, 79 (2009).

[11] S. G. Rohoziński, L. Próchniak, K. Starosta, and C. Droste, Eur. Phys. J. A **47**, 90 (2011).

[12] N. J. Stone, At. Data Nucl. Data Tables **90**, 75 (2005).

[13] P. J. Brussard and P. W. M. Glaudemans, *Shell-Model Applications in Nuclear Spectroscopy* (North-Holland, Amsterdam, 1977).

[14] *Relativistic Density Functional for Nuclear Structure*, edited by J. Meng (World Scientific, Singapore, 2016).

[15] J.-M. Yao, J. Peng, J. Meng, and P. Ring, Sci. China Phys. Mech. Astron. **54**, 198 (2011).

[16] J. Li, J. X. Wei, J. N. Hu, P. Ring, and J. Meng, Phys. Rev. C **88**, 064307 (2013).

[17] P. Raghavan, At. Data Nucl. Data Tables **42**, 189 (1989).

[18] K. Starosta, T. Koike, C. J. Chiara, D. B. Fossan, and D. R. LaFosse, Nucl. Phys. A **682**, 375 (2001).

[19] P. Olbratowski, J. Dobaczewski, J. Dudek, and W. Plociennik, Phys. Rev. Lett. **93**, 052501 (2004).

[20] J. Peng, J. Meng, and S. Q. Zhang, Phys. Rev. C **68**, 044324 (2003).

[21] S. Q. Zhang, B. Qi, S. Y. Wang, and J. Meng, Phys. Rev. C **75**, 044307 (2007).

[22] B. Qi, S. Q. Zhang, J. Meng, S. Y. Wang, and S. Frauendorf, Phys. Lett. B **675**, 175 (2009).

[23] Q. B. Chen, B. F. Lv, C. M. Petrache, and J. Meng, Phys. Lett. B **782**, 744 (2018).

[24] Q. B. Chen, N. Kaiser, Ulf-G. Meissner, and J. Meng, Phys. Rev. C **99**, 064326 (2019).

[25] Q. Chen, N. Kaiser, U.-G. Meissner, and J. Meng, Phys. Lett. B **807**, 135568 (2020).

[26] Q. B. Chen, S. Frauendorf, N. Kaiser, U.-G. Meissner, and J. Meng, Phys. Lett. B **807**, 135596 (2020).

[27] C. Broocks, Q. B. Chen, N. Kaiser, and U.-G. Meissner, Eur. Phys. J. A **57**, 161 (2021).

[28] S.-Y. Wang, B. Qi, and S.-Q. Zhang, Chin. Phys. Lett. **26**, 052102 (2009).

[29] J. Meng, J. Peng, S. Q. Zhang, and S.-G. Zhou, Phys. Rev. C **73**, 037303 (2006).

[30] P. W. Zhao, Z. P. Li, J. M. Yao, and J. Meng, Phys. Rev. C **82**, 054319 (2010).

[31] A. Arnesen, K. Johansson, E. Karlsson, T. Noreland, L.-O. Norlin, and S. Ogaza, Hyperfine Interact. **5**, 81 (1977).